		A1	A2	A3	A4	A5
Mass	[kg]	7768	10100	24938	45479	88623
Available volume	[m³]	10	13	52	100	182
Flying range	[km]	1910	1350	1940	3040	2580
Max L/D	[-]	0.26	0.17	0.116	0.10	0.03
Max g-load	[-]	6.9	7.9	5.2	4.5	7.7
Max heat-flux	[MW/m²]	0.772	0.654	0.672	0.633	1.0
Max temperature nose	[K]	2250	577	2150	2160	2300
Max temperature rear part	[K]	700	897	900	919	1030
Max temperature bond-line	[K]	550	423	547	600	460

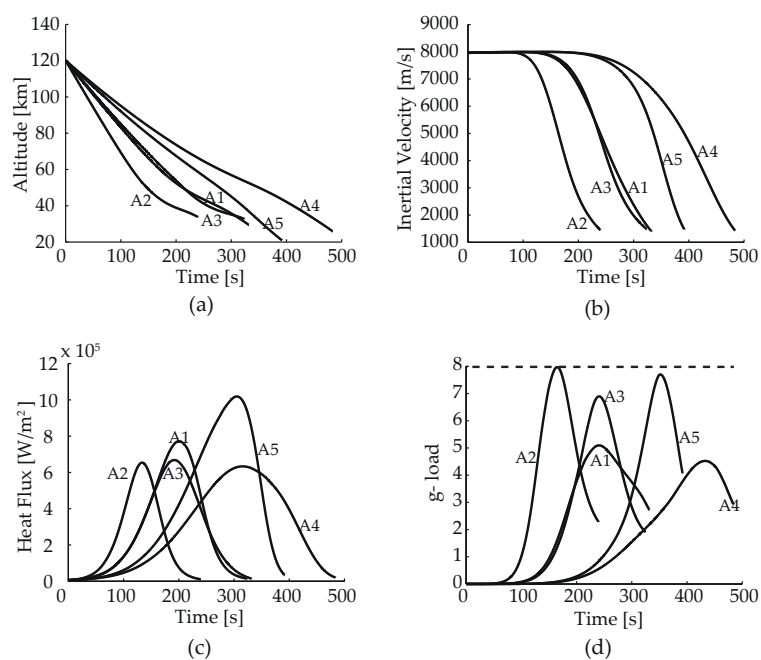Table 5.3   Reusable capsules summary of the most relevant performance.

Figure 5.17   Performance of the capsules A1 to A5.

cool is almost 8% of the entire capsule mass. Further, the nose thickness results to be rather large, see Table 5.2. This means that, for the given design parameters ranges, to obtain a metallic water-cooled capsule nose that meets the temperature constraints there has to be quite a relevant amount of water coupled with a bulky skin that will absorb and store part of the incoming heat. Even if a large amount of water may be required, water-cooling is still a quite effective mechanism for releasing the incoming heat. In Figure 5.18 the temperature trends of capsule A2, show indeed that even with a peak heat flux that is comparable to that experienced by capsule A3, the water cooling mechanism at the nose allows the temperature to be much lower, thus making the capsule more *reusable*, according to the definition we have given here, by keeping the temperature of the metallic material far from its operating-limit temperature.

The heat-sink mechanism, represented by the metallic uncooled solution, is not as efficient as the others. There are very few capsules on the Pareto front with this solution, and all of them have a heat-sink only on the rear part, where the heat-flux is significantly lower (considered 30% of the stagnation heat-flux (Wright *et al.*, 2006)). Capsule A1 is representative for these capsules. As presented in Table 5.2 the thickness of the rear part is relatively large. This makes the TPS in general heavy. Unlike the other *metallic* solutions, the enhanced-radiation cooling-mechanism for the rear part of the capsules *survives* in the optimization process even
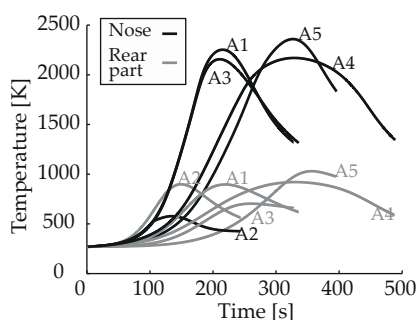
Figure 5.18   Nose and rear part temperature profiles for the outer skin of the capsules A1 to A5.

for large capsules having a large rear-part exposed surface. This is mostly due to the fact that this unconventional approach to keep a metallic surface cool allows the skin thickness to be very small and still requiring a limited amount of water when compared to the direct water-cooling mechanism. Ultra High Temperature Ceramics, of which ZrB2-SiC is only one example, perform very well in terms of mass-volume efficiency. In general, a thin skin can provide good performance in terms of maximum temperature reached by the material, even with very large nose and rear part surfaces.

5.5.2   Robust optimization

In this section the results obtained using the robust-optimization approach with recursive sampling and adaptive selection introduced previously in this chapter are described. The capsules obtained with the robust optimization will not be just a robust version of the capsules analyzed in the previous section, but rather the most robust-optimal ones on the entire search space that the robust-optimizer was able to provide. The uncertain factors used for the robust optimization are described in Table 5.4. The objective of this analysis is to illustrate the proposed methodology for robust optimization. To that end, an attempt was made to select reasonable values for the uncertainties; however these values are for illustration only. The robust Pareto front has been obtained with an optimization process using 300 generations and 150 as population size. To compute robustness, for each point in the design space 100 sample points are generated to estimate the joint PDF. With no measures to reduce the computational cost, this analysis would have lead to 4.5 million model evaluations. Considering that each single model evaluation takes 10 seconds to execute, the total computational cost would be around 17 months CPU time. The double-repository archive maintenance scheme allowed to reduce the computational cost to circa 2 months CPU time, with around 675,000 model evaluations. In this analysis, the initial entry velocity is the only uncertain factor that is not also a design variable. This means that its variation is independent from the current position of the design point in the design space. Therefore, the boundaries for the initial velocity are fixed, while the boundaries for the other four uncertain factors are given as a minimum and maximum variation around the current design point. The initial velocity and initial flight-path angle uncertainties are considered to take any possible uncertainty coming from injection conditions into account. The uncertainty related to the position of the center of mass is meant to account for uncertainties related to manufacturing of the capsules and subsystems placement for subsequent phases of the design cycle. Finally, the uncertainty related to the thickness of nose and rear part thermal protection systems will encompass all uncertainties related to the accuracy of the 1D thermal model, material properties, and incoming heat flux. These uncertainty boundaries may seem large, however it shall be noted that they represent the 99 percentile of the uncertainty distribution, and that similar uncertainty values can be found in the literature given uncertainty in material density, and thermal properties (Mazzaracchio and

Uncertain Parameters		Intervals		Distribution
		Min	Max	
Z-position CoM[a]	[m]	-0.01125	$+0.01125$	Normal
Thickness Nose[a]	[m]	-0.002	$+0.002$	Normal
Thickness rear part[a]	[m]	-0.002	$+0.002$	Normal
Initial flight-path angle[a]	[deg]	-0.5	$+0.5$	Normal
Initial inertial entry velocity	[m/s]	7885	7985	Log-Normal[b]

Table 5.4   Settings of the uncertain factors.[a] In this case the Min and Max represent the minimum and maximum deviation from the nominal value, which varies with the design point position in the design space. Min and Max are the 0.01 and 0.99 percentile respectively. [b] Min is the 0.99 percentile, Max corresponds to $X = 0$, *i.e.*, the maximum value never exceeded by the log-normal distribution.
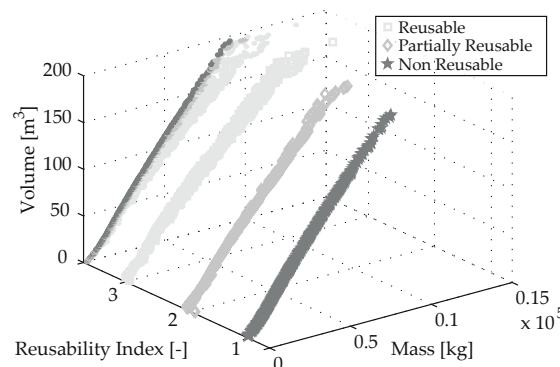

Figure 5.19   Complete Pareto front obtained with the robust-optimization, robotic capsules servicing the ISS.

Marchetti, 2012). The capsules obtained with this optimization process shall be interpreted as those that do not violate the constraints with 99% confidence and that still have an efficient mean performance in terms of mass, volume, and re-usability.

The results of the robust-optimization are presented in Figure 5.19. The complete robust Pareto front resembles the Pareto front of Figure 5.16, obtained with the non-robust optimization process. This is expected since the uncertain factors do not actually affect the separation between fully reusable, partially reusable, and non-reusable thermal-protection systems. One general feature that can be observed in Figure 5.19 is the reduced efficiency that the fully reusable capsules have when compared to the partially reusable capsules. These are in turn less efficient than the non-reusable ones. This can be observed in the projections of the solutions on the Mass-Volume plane, where the branch of the Pareto front with the non-reusable capsules is *higher* than the other two branches. This phenomenon was not present in the original Pareto front where the three branches were aligned on the Mass-Volume plane, besides some trade-offs between mass and re-usability for the fully reusable capsules. This feature can, in general, be translated into a reduced sensitivity of the ablative materials to the uncertainties of Table 5.4, that in turn means that non-reusable capsules are more robust and closer to the optimal conditions even in the presence of these type of uncertainties.

As done previously, in Figure 5.20 we focus the attention on the branch of the robust Pareto front with reusable capsules. The projection of both the robust Pareto front (gray dots) and the Pareto front of Figure 5.16 (black dots) is on the mass-volume plane. As shown in the magnified portion of Figure 5.20, the optimal-robust solutions are less efficient in terms of performance when compared to the original Pareto-optimal solutions. However, the Pareto-optimal solutions present worse constraint-violation conditions when the uncertainties of Table 5.4 are taken into account. Capsule B1, for instance, presents average performance that is close to

		B1	B2	B3
Nose radius	[m]	4.97	4.92	4.96
Corner radius	[m]	0.34	0.21	0.29
Rear part angle	[rad]	−0.6	−0.47	0.15
Capsule radius	[m]	2.7	4.0	4.5
Capsule length	[m]	0.54	0.67	2.9
Z-position CoM	[m]	0.07	0.082	0.048
Type of TPS nose	[-]	ZrB2-SiC	ZrB2-SiC	ZrB2-SiC
Thickness Nose	[m]	0.0074	0.002	0.014
Type of TPS rear part	[-]	Enhanced radiation cooling	ZrB2-SiC	Enhanced radiation cooling
Thickness rear part	[m]	0.002	0.0015	0.0079
Initial water-mass nose	[kg]	-	-	-
Initial water-mass cone	[kg]	80	-	180
Initial flight-path angle	[deg]	−3.61	−2.22	−2.58
Initial bank angle	[deg]	29	90	14

Table 5.5   Robust-reusable capsules design parameters settings.

the performance of capsule A2, even though it is heavier and with less available volume for payload. However, when subjected to the uncertain conditions described before, capsule B2 proves to be a much better solution than capsule A2. Indeed, as presented in Figure 5.21 the temperatures reached by the TPS parts are well below the material limits, and also the g-load of the capsule is far from the 8g limit. This is not the case for capsule A2.

Under the influence of the uncertain conditions of Table 5.4 there is the chance that the capsule will not meet the g-load constraint and that the water needed to cool the nose will exceed the actual water within the capsule, as shown in Figure 5.22. The robust-optimization pushes the robust Pareto front away from the original Pareto front as shown in the zoom in Figure 5.20, in a similar fashion to the test problems shown before. The effect is that for a given volume, the capsules are heavier. This is driven by the fact that the average thickness of the TPS of both nose and cone gets higher. This effect is actually due to several causes. First of all, in general the trajectories are steeper, meaning that the initial flight-path angle gets more negative. This effect, coupled with a reduced shift of the center of mass causes the maximum g-load to decrease as well as the flight range of the capsules. This decreases the heat load thus providing more robustness in terms of *material consumption*. However, the maximum heat flux

		B1	B2	B3
Mass[a]	[kg]	11150	25550	75275
Available volume[a]	[m³]	12.89	55	142
Flying range[a]	[km]	1704	2337	2274
Max Cl/Cd[a]	[-]	0.21	0.12	0.06
Max g-load[b]	[-]	5.7	7.9	7.7
Max heat-flux[b]	[MW/m²]	0.71	0.76	1.15
Max temperature nose[b]	[K]	1890	2250	2350
Max temperature rear part[b]	[K]	737	812	930
Max temperature bond-line[b]	[K]	460	560	456

Table 5.6   Robust-reusable capsules summary of the most relevant performance. [a]Values of the nominal capsule. [b]Values with 99.9% confidence.

increases thus leading to a higher temperature of the external skin. This is true especially for fully reusable and partially re-usable capsules.
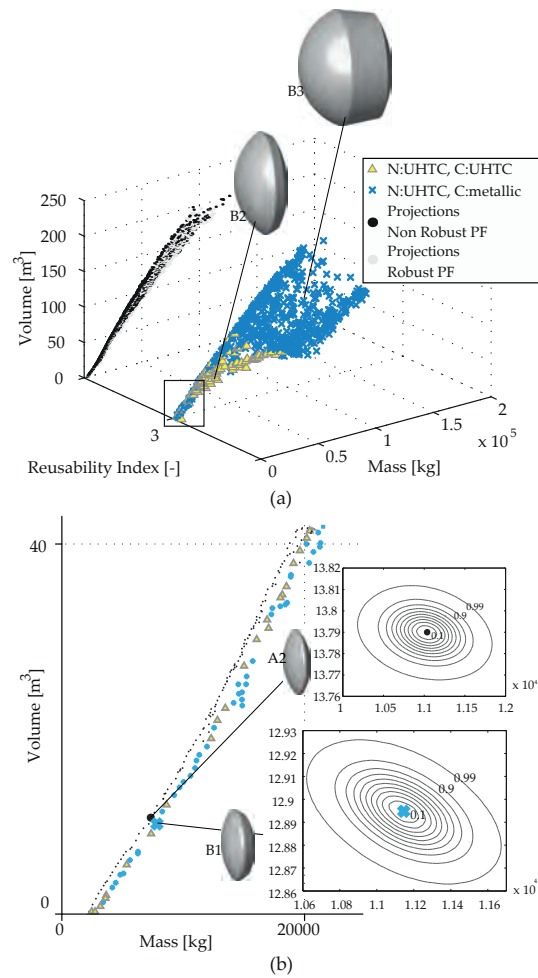

Figure 5.20   Robust Pareto front with fully re-usable capsules, robotic capsules servicing the ISS.

Non-reusable capsules, having both nose and rear part of ablative material, show a more robust behavior, also in terms of maximum external-skin temperature. The trends introduced here have been quantitatively shown in Figures 5.23 to 5.26.
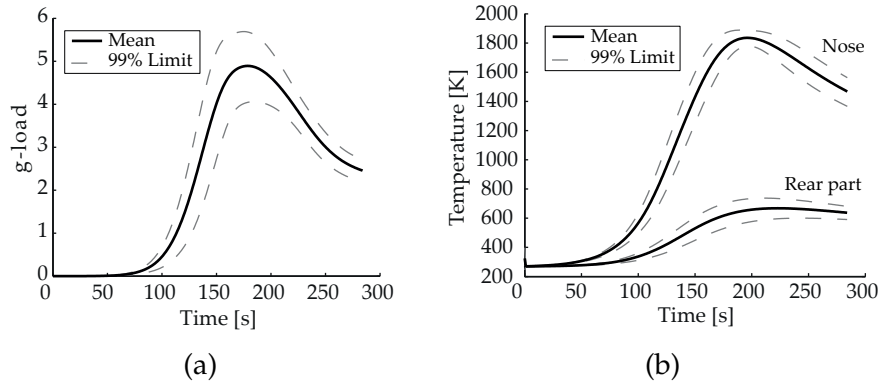
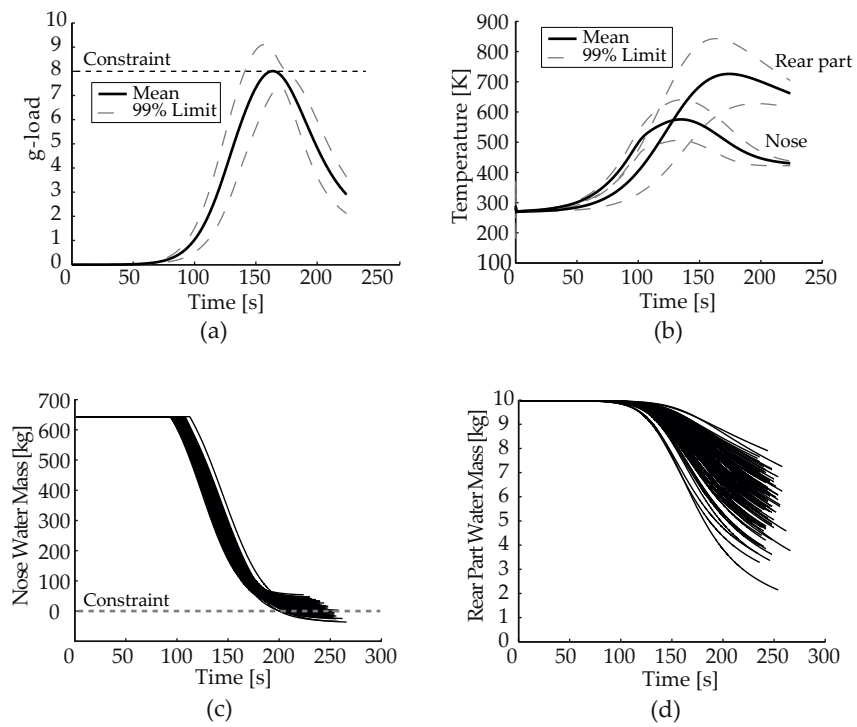Figure 5.21   Performance of the capsule B1 under uncertain conditions.

Figure 5.22   Performance of the capsule A2 under uncertain conditions.